Understanding crystal surface anisotropy of organic materials via molecular modelling and facet-specific experimental characterization

Original
Understanding crystal surface anisotropy of organic materials via molecular modelling and facet-specific experimental characterization / Prandini, Emilia; Torre, Bruno; Bosurgi, Emanuele; Maloney, Andrew G. P.; Stani, Chiaramaria; Birarda, Giovanni; Vaccari, Lisa; Fabrizio, Enzo Mario Di; Parisi, Emmanuele; Simone, Elena. - In: APPLIED SURFACE SCIENCE ADVANCES. - ISSN 2666-5239. - 32:(2026), pp. 1-14. [10.1016/j.apsadv.2026.100939]

Availability:
This version is available at: 11583/3008931 since: 2026-03-19T13:14:27Z

Publisher:
Elsevier

Published
DOI:10.1016/j.apsadv.2026.100939

Applied Surface Science Advances 32 (2026) 100939

Contents lists available at ScienceDirect

Applied Surface Science Advances

journal homepage: www.sciencedirect.com/journal/applied-surface-science-advances

Full Length Article

Understanding crystal surface anisotropy of organic materials via molecular modelling and facet-specific experimental characterization

Emilia Prandini [a], Bruno Torre [b], Emanuele Bosurgi [a], Andrew G.P. Maloney [c], Chiaramaria Stani [d], Giovanni Birarda [d], Lisa Vaccari [d], Enzo Mario Di Fabrizio [a], Emmanuele Parisi [a], Elena Simone [a,*]

[a] Department of Applied Science and Technology (DISAT), Politecnico di Torino, Corso Duca degli Abruzzi, 24, 10129, Torino, Italy
[b] Istituto Nazionale di Ricerca Metrologica (INRiM), Str. delle Cacce, 91, 10135, Torino, Italy
[c] The Cambridge Crystallographic Data Centre, 12 Union Road, CB2 1EZ, Cambridge, United Kingdom
[d] Elettra Sincrotrone Trieste, Strada Statale 14, 34149, Trieste, Italy

ARTICLE INFO

Keywords:
Surface chemistry
Crystal engineering
Crystal anisotropy
Particle Informatics
OPTIR
AFM
s-SNIM

ABSTRACT

The different facets of crystalline particles expose specific functional groups depending on their structure and morphology, thus, influencing surface properties of the resulting materials. As particle surface properties impact product performance, safety, and manufacturing efficiency, it is important to understand how crystal structure influences facet-specific surface properties. In this work, we focused on the effect of crystal structure and morphology on properties such as roughness, mechanical strength, and chemical features. Quercetin-dimethylformamide (QDMF), a solvated form of quercetin, was selected as a single-crystal model compound. By combining computational approaches with experimental validation, we developed a standardized procedure to correlate crystal structure packing and specific surface features. Experimental data collected using various techniques were then used to validate the simulations.

First, we utilized Particle Informatics tools to analyse the surface chemistry and topology of specific QDMF crystal facets observed experimentally, namely {1–10}, {001}, and {200}. These computational results were then validated using Atomic Force Microscopy (AFM) integrated with Infrared (IR) spectroscopy, which provided topographical insights, chemical characterization, surface roughness measurements, and mechanical properties characterization (e.g., Young Modulus).

For chemical imaging at high spatial resolution, we employed advanced mid-infrared techniques, such as Optical Photothermal Infrared (OPTIR) microscopy and scattering-type Scanning Near-field Infrared Microscopy (s-SNIM). The experimental data were in agreement with the simulations, showing how Particle Informatics tools can assist in the design of crystalline materials with tailored surface properties.

Introduction

Crystalline materials can exhibit anisotropy across different crystallographic planes due to the directional nature of their molecular packing and intermolecular interactions [1–3]. Due to this anisotropy, several structural (defect density, slip planes) [4–6], mechanical (thermal expansion, elasticity, plasticity, and hardness) [7–20], physical (optical properties and electronic transport) [21–24], and chemical (surface energy, reactivity, and wettability) [25–30] properties depend on the orientation of the molecules on the exposed crystal surfaces. Among those properties, wettability, surface energy, plasticity, and elasticity directly impact product quality in several sectors including pharmaceuticals [31,32], electronics [33,34], and energy storage [35]. In pharmaceutical, for example, they influence key product quality attributes such as rate of dissolution and bioavailability, processability, and stability (e.g., tendency to adsorb humidity and pack during storage, or tendency to de-solvate/dehydrate) of fine chemical, agrochemical and pharmaceutical particles [36–40]. Facet specific properties are also relevant for advanced optical material design; in fact, a recent work on wafer-scale porphyrin derivatives shows that optical birefringence can be tuned independently of spectral response simply by controlling which crystal planes are exposed in the final material [41]. Bade et al. showed

---

* Corresponding author.
E-mail address: elena.simone@polito.it (E. Simone).

https://doi.org/10.1016/j.apsadv.2026.100939
Received 22 November 2025; Received in revised form 19 January 2026; Accepted 20 January 2026

that two batches of the osteoporosis drug candidate Odanacatib, prepared either via precipitation or jet-milling, exhibit identical particle-size distributions yet sharply different dissolution and flow profiles; these differences were traced to process-induced differences in the surface of Odanacatib crystals [42]. Comparable effects can now be predicted in silico from lattice-specific binding energies, and have been linked to inequivalent wetting and facet-specific dissolution rates for single-crystal APIs [43]. The nature of a crystal facet also governs its interactions with solvents, additives, and impurities during crystallization and downstream operations, as well as unwanted interactions with relevant environments during storage and after administration.

Crystal morphology can be controlled during crystallization, through process parameters, in several ways, including an appropriate choice of solvent [44] and/or thermal profile [45–46] (e.g., consecutive cycles of growth and dissolution), and particle breakage [47]. The recent development of theoretical models to describe morphological crystal growth [48,49] allows a precise tuning of particle morphology with tuned surface properties.

Facet-specific properties are strongly linked to crystal structure [50], in particular to the nature and directionality of the intermolecular interactions within the crystal lattice. Understanding how these interactions translate into facet-specific chemistry and then surface-related properties (e.g., wettability, mechanical response) is therefore essential for rational design of crystalline materials with tailored surface properties [51–53]. For instance, Muster et al., work on N,N-octyl-ᴅ-gluconamide and sulfathiazole forms I and III, showed how facet-specific surface energy and wettability correlate with crystal structure and chemistry, using contact angle measurements and AFM analysis [50]. Cao et al., analysed the three-dimensional topography and adhesion properties of sulfamerazine single crystals, forms I and II, utilizing AFM and Raman spectroscopy. AFM offered detailed insights into crystal size, surface morphology, roughness, and edge characteristics [54], while Raman was used for structural characterization.

Several studies on inorganic crystalline surfaces have established robust methodologies for integrating Atomic Force Microscopy (AFM) with atomistic simulations to rationalize facet-specific interfacial properties. Kim et al. demonstrated how hydroxyl and carboxyl functional groups alter calcite surface wettability by combining AFM measurements with differential functional theory (DFT) simulations [55]; while Chai et al. systematically investigated the adsorption of representative organic molecules on calcite surfaces through AFM, Fourier Transform IR spectroscopy (FTIR), and DFT, elucidating the interaction mechanisms in atomic scale [56]. Comparable frameworks have also been applied to graphitic and carbon-based surfaces, where DFT and molecular dynamics simulations combined with AFM revealed how interfacial water organization governs nanoscale adhesion and apparent wetting behaviour [57]. These studies showed that nanoscale adhesion and the organization of interfacial water govern macroscopic trends in wettability, while also clarifying the known limitations of contact-angle measurements on heterogeneous or nanorough surfaces [58]. Together, these contributions highlight that robust methodologies linking atomistic simulations, AFM measurements, and macroscopic interfacial phenomena are already well established for inorganic and carbon-based systems. By contrast, their application to organic molecular crystals remains largely unexplored and constitutes a primary focus of the present work. In summary, several critical technical challenges continue to limit the broader application and overall effectiveness of both computational and experimental surface characterization techniques [59]. Many experimental surface characterization techniques provide high resolution and sensitivity, but are not suitable for routine particle properties measurements due to complex sample preparation procedures and time-consuming measurements. AFM and s-SNIM or nano-Raman spectroscopy are two evident examples, as they provide rich, physical, and chemical information of surfaces, but require rigorous and time-consuming sample preparation protocols. Obtaining single, organic crystals of sufficient size and quality is essential to enable facet-specific analysis and adds further complexity to the experimental workflow. Moreover, another major hurdle in the field is the development of hybrid analytical instruments that integrate multiple complementary characterization techniques into a single platform, for example, AFM for physical characterization and Raman/IR for chemical information. Such instruments enable simultaneous acquisition of diverse data types, providing a more comprehensive understanding of the nature of the surface under analysis. Recent developments in AFM have incorporated complementary analytical methods such as Raman spectroscopy, Infrared spectroscopy (IR), and confocal microscopy, thereby expanding its ability to reveal chemical composition and map chemical distribution on sample surfaces [60–62]. In this context, developing computational methods to simulate and predict facet-specific properties of organic crystalline materials can significantly accelerate product development by reducing dependence on lab-intensive experimental protocols and enabling early prediction of facet-specific properties directly from crystal structures. Hence, this work aims to develop computational tools and experimentally validated procedures to predict surface properties, starting from structural information of the analysed material. In particular, we attempt to establish clear correlations between structural motifs and facet-specific properties in order to enable rational material design for crystalline particles. Experimental validation was also performed. This was not a trivial task, as to analyse individual facets of an organic crystal, large, perfect single crystals are needed, and then their exact orientation must be determined. For this purpose, a combination of high-resolution surface characterization techniques has to be determined to obtain the required information. In particular, we adopted an integrated approach that combines facet-specific experimental characterization with an effective synthesis method for obtaining single crystals of the desired size, enabling high-resolution surface analysis. AFM was coupled with Infrared spectroscopic measurements (s-SNIM) to simultaneously capture topographical, mechanical (elastic modulus, stiffness, and indentation depths) and chemical information at the crystal facets [63–68]. OPTIR microscopy was used to obtain surface sensitive chemical data at lower lateral resolution (500 nm) [64]. Particle-Informatics modelling was used for prediction, visualization, and experimental verification of the structural and chemical features unique to different crystal facets [69, 70]. A solvated structure of quercetin, quercetin-dimethylformamide (QDMF), was selected as a model system for this work because it forms large, well-defined single crystals exposing multiple experimentally accessible crystallographic facets, which can be reliably indexed and individually probed with surface-specific characterization techniques. Previous study performed on this compound highlighted the possibility to predict particle quality attributes through Particle Informatics modelling. Here, we focused particularly on the experimentally relevant crystallographic facets {1–10}, {001}, and {200} of QDMF. Simulated facet chemistries of QDMF were compared with experimental measurements using AFM Amplitude Modulation (AM) and Frequency Modulation (FM), s-SNIM and OPTIR, with AM-FM AFM providing well-established nanoscale mapping of mechanical properties, including elastic modulus [71,72].

This integrated approach involves a combination of structural motifs (such as hydrogen bonding patterns, aromatic exposure, and intrinsic properties) prediction and experimental estimation of chemical and mechanical properties at the micro- and nanoscale. Unlike previous Particle Informatics studies, which typically remain unvalidated at the level of individual facets, our workflow provides a standardized, facet-resolved correlation between crystal packing and surface properties.

To summarize, a comprehensive characterization of how distinct crystal facets behave structurally and functionally can provide the basis for targeted surface modification, selective facet stabilization, or morphology control strategies aimed at enhancing performance or reproducibility.

Materials and methods

Materials

Quercetin dihydrate (QDH) (97 % purity) was obtained from Thermo Fisher Scientific (Kandel, Germany) and used as received. N, N-dimethylformamide (DMF) solvent was purchased from Sigma Aldrich (Steinheim, Germany).

Preparation of quercetin-dimethylformamide (QDMF) single crystals

The quercetin dimethylformamide solvate (QDMF) was prepared by pouring 300 mg of QDH in a jacketed vessel with 470 mg of DMF. The temperature was increased from 20 °C to 80 °C at a rate of 0.5 °C/min to facilitate complete dissolution of the solid. Subsequently, the solution was cooled down to room temperature at a rate of −0.5 °C/min using the multi-reactor crystallizer Crystal16® V2 (Technobis Crystallization Systems, Alkmaar, The Netherlands). The solution was stirred continuously using an overhead stirrer at 780 rpm. Following nucleation, the vials containing the solution were left open under ambient conditions for a minimum of five days, to allow solvent evaporation and facilitate crystal growth.

Surface chemistry and topology modelling and simulation

The QDMF bulk structure and facet-specific properties were calculated using the software Materials Studio 2021(v21.1.1.3268) and Mercury CSD 2025.1.1 on our previously solved and deposited structure (Refcode in CSD: ZUWGEH). Mercury was also used for the visualization of structural and facet-specific features of QDMF. The structure minimization and the optimization of unit cell parameters were performed using the Forcite module in Materials Studio 2021. The torsion angle between the phenyl and pyrone moieties was kept rigid. The SMART algorithm was selected for the structural minimization with the Dreiding II forcefield. With this forcefield, van der Waals interactions are described by the Lennard-Jones potential, whereas electrostatic interactions are described by atomic monopoles and a screened (distance-dependent) Coulombic term. Finally, hydrogen bonding is described by an explicit Lennard-Jones 12–10 potential.

The calculation of the intermolecular interactions and intrinsic synthon analysis were carried out with the VisualHabit module [73–75] in the CSD-Particle suite in Mercury, applying the same Dreiding II forcefield. This module applies the attachment energy model to determine which synthons contribute to the growth of each facet and to estimate facet-specific properties such as rugosity, densities of H-bond donors, H-bond acceptors, and aromatic bonds. These facet-specific descriptors provide a quantitative illustration of the chemical and topological anisotropy of the crystal surfaces, directly reflecting the intermolecular interactions that contribute to the growth of each facet. By linking the dominant growth synthons to the exposed functional groups and surface roughness of each plane, it is possible to interpret particle morphology in terms of surface chemistry and intermolecular bonding patterns that are relevant for crystal growth and interfacial behaviour. Additionally, a CSD Python API script (https://github.com/ccdc-opensource/science-paper-quercetin-DMF-surface-analysis-2024) was used to perform a detailed surface chemistry analysis. This script examines the individual surface nodes constituting each topological surface, calculating the percentage of surface area associated with each atom type. Due to minor overlaps among these surface nodes, the total calculated percentage for all atoms may not equal exactly 100 %. The three modelled surfaces are (110) with an offset of −2.56, (002) with an offset of −1.81, and (200) with an offset of 0. The offset represents the value in Å of the distance to the calculated surface from the parallel Miller plane, and these values were obtained from the VisualHabit calculation. Only facets that were experimentally identified on the QDMF crystals were considered for the facet-specific surface analysis, as shown in our previous work [69].

Attenuated total reflection Fourier Transform infrared spectroscopy (ATR-FTIR)

The QDMF and QDH powders were analysed with ATR-FTIR. Spectra were collected on a Bruker Tensor 27 spectrometer. Samples were measured from 800 to 1800 $\mathrm{cm^{-1}}$ at a resolution of 4 $\mathrm{cm^{-1}}$ and accumulating 64 scans. The data was processed using the Opus 8.2.28 software.

Optical photothermal infrared spectroscopy (O-PTIR)

Single crystals of QDMF freshly taken out from solution and cleaved carefully with a razor blade were analysed using a mIRage-LS microscope (Photothermal Spectroscopy Corporation, USA) equipped with a hyperspectral quantum cascade laser (QCL) in the range between 1800 and 800 $\mathrm{cm^{-1}}$, a 532 nm detection laser, a 40 × all-reflective Cassegrain objective (0.78 numerical aperture, 8 mm working distance), and a silicon avalanche photodiode detector. OPTIR spectroscopy enables chemical characterization of samples with sub-micron resolution, independent of the wavelength. A pulsed IR laser induced localized photothermal effects, with IR absorption causing thermal expansion or refractive index changes, probed by the 532 nm laser (power 0.26 % of ∼60 mW) to the sample for high-resolution detection. The IR and probe lasers were collinear and focused via an optical objective (40X magnification), with backscattered green light analysed to extract the IR absorption signal. OPTIR spectroscopy is characterized by a spatial and axial resolution that are independent of the wavelength, and much higher than traditional IR microscopy (Figure. S1 in the Supporting Information). The theoretical spatial and axial resolutions for the setup used in this work are 0.416 and 1.7 µm. It is worth noting though, that backscattered light collected by the detector is limited to the sample surface. Laser tuning was regulated at 1649 $\mathrm{cm^{-1}}$ (IR Power = 5 % of ∼50 mW, pulse rate 100 kHz and duty cycle 1 %), which corresponds to a strong absorption band of QDMF observed in the ATR-FTIR spectrum. Spectra were acquired averaging 8 consecutive scans, with a spectral resolution of 6 $\mathrm{cm^{-1}}$ and spectral sweep speed of 10^3 $\mathrm{cm^{-1}s^{-1}}$. Data analysis was performed using the commercial software PTIR Studio 4.6 and Python version 3.13. Normalization of spectra was carried out considering the peak at 1655 $\mathrm{cm^{-1}}$.

Scattering-type scanning near-field infrared microscopy (s-SNIM)

The same samples analysed with OPTIR were also studied via s-SNIM microscopy. The instrument used (Attocube Systems AG, Germany) was operating in scattering-type Scanning Near-field Infrared Microscopy (s-SNIM) mode. This technique combines AFM, operated in tapping mode, and an asymmetric Michelson interferometer, enabling nanoscale chemical characterization beyond the diffraction limit of conventional FTIR. A metal-coated AFM tip was illuminated by a broadband mid-IR laser, and acting as a nano-antenna, the tip concentrated the IR field to a nanometric region of the sample. The backscattered IR light, modulated at the AFM tapping frequency and higher harmonics, was detected interferometrically to extract near-field IR spectra and images with nanometer spatial resolution. Topography and near-field IR signals were acquired simultaneously, allowing for correlative structural and chemical analysis. Spectral processing and data analysis were performed using Neaspec control software and Python version 3.13.

Bi-modal atomic force microscopy (AFM)

To understand surface and interfacial properties of QDMF, we employed AFM in Amplitude Modulation-Frequency Modulation (AM-FM) mode, one of the most versatile tools for that purpose. This technique enables high-resolution topographical imaging in Amplitude

Modulation mode while simultaneously mapping mechanical properties using Frequency Modulation on a higher eigenmode, providing stiffness and elasticity maps with nanometer resolution. In particular, this approach provides quantitative information on the Young modulus of the sample.

Single crystals of QMDF were taken out of solution and cleaved under controlled environmental conditions of 24 °C. AFM measurements were performed using a MFP-3D Stand Alone AFM (Asylum Research, Oxford Instruments) equipped with AM-FM holder optimized for nanomechanical analysis. All images were obtained using AC160TS-R3 cantilever probes (Olympus), with nominal spring constant (k) and tip radius of this cantilever are 26 N/m and 7 nm, respectively. Before imaging and mechanical mapping, the tip was calibrated using thermal noise method to determine the cantilever spring constant, while the inverse optical lever sensitivity (InvOLS) was obtained from force curve measurements acquired on a silicon reference sample, using Sader method [76,77]. During the experimental procedure, the parameters were set at these values: free amplitude 2 V, setpoint 600 mV, scan size 5 μm and 2 μm, resolution 256 points × 256 lines, scan rate 0.20 Hz, and scan angle 90° Then, under cantilever tuning the primary mode was set with a free amplitude of 2 V, with a target percentage tolerance of −5 %, and the secondary mode was set with a free amplitude of 25 mV. The low and high tuning ranges were defined between 280 kHz and 1.6 MHz, ensuring it remained within 1.5–1.9 MHz. The phase was centred for both resonance modes. The optimization of the second amplitude was performed adjusting the laser spot onto the cantilever tip to maximize the amplitude. A single force curve measurement was acquired setting the force distance at 500 nm, with trigger point of 800 mV. Following force calibration, both resonance frequencies were retuned. During all measurements surface indentation was limited to 1 nm or less. Young modulus was retrieved using Hertz model calculation with tip radius of 7 nm and poisson ratio of 0.27. The topography images, Young modulus images, and Young modulus map obtained were processed using Python version 3.13.

Scanning electron microscopy (SEM)

The morphology of QDMF crystals was examined using a Quanta 3D FEG 200i operating at a 30 kV voltage with a variable beam current between 100 and 250 pA. For SEM specimen preparation, single crystals freshly taken out from solution were mounted on carbon tape attached to metal stubs. Crystals were positioned along the (200) and (001) crystallographic planes determined after X-ray indexing, without additional preparation. To enhance conductivity and imaging quality, the samples were coated with a platinum layer for 30 s before analysis.

Powder X-ray diffraction and single crystal X-ray indexing

Single crystal indexing, before SEM, OPTIR and s-SNIM, was performed on a Gemini R Ultra diffractometer (Agilent Technologies UK Ltd., Oxford, U.K.) using Cu Kα radiation (λ = 1.5406 Å)) with the ω-scan method. The facet indexing of the crystal sample was carried out using CrysalisPro (v.171.42.49, Rigaku Oxford Diffraction) software. Powder X-ray diffraction, before bulk ATR-FTIR, was instead conducted on a PANalytical Empyrean x-ray diffractometer, equipped with Bragg-Brentano HD optics, a sealed tube copper X-ray source, using a Cu Ka radiation fitted with a PixCel3D Medpix detector. The sample was scanned between 3° and 40° in 2θ with a step size of 0.01313° (2θ) and a time per step of 100 s. The X-ray generator was set at a tube voltage of 40 kV and a current of 40 mA. Samples were prepared with a Si zero background and measured without spinning.

Mechanical properties calculation

In order to calculate the Young modulus, molecular mechanics simulations were performed with Materials Studio 2021 v. 21.1.0.3268 on the optimized crystal structure of QDMF. A 4 × 4 × 4 unit cell was generated with P1 symmetry by replicating the unit cell along each lattice vector. The symmetry reduction to the *P*1 space group allows calculation of all 21 independent components of the elastic tensor by avoiding approximation for symmetry. Defects, local distortions, and elastic waves do not interact with their replica within an 18.5 Å cutoff, improving the accuracy of elastic constants and moduli. We have enlarged the unit cell block to better represent experimental behaviour, enabling small strains (≤ 0.3 %) without size-dominated artifacts. The Dreiding II forcefield used was the same as the optimization step.

Chart. 1 schematically summarizes the modelling and experimental workflows used in this paper.

Results and discussion

QDMF simulated surface features

The unit cell packing, the asymmetric unit, and the crystallographic data of the QDMF crystal structure are reported in Figure. S2 and Table S1 of the SI file.

Experimentally indexed crystals of QDMF were characterized by three predominant facets: {1–10} constitutes 55 % of the total crystal surface, while {001} and {200} contribute for the remaining 22 % and 23 %, respectively (Fig. 1).

In our previous work, using the attachment energy model, it was determined that the primary interaction driving the growth of the experimental {001} facet is a stacking interaction between quercetin molecules. In contrast, for the other two experimental facets, {1–10} and {200}, crystal growth is dominated by hydrogen bonding between quercetin-quercetin and quercetin-DMF molecules. The topology of these three facets was simulated using the CSD-Particle suite in Mercury and is reported in Fig. 1, where hydrogen bond donor and acceptor sites are highlighted in blue and red, while the aromatic bond sites are coloured in orange. It is evident that the absence of aromatic contribution to the {1–10} facets is due to the orthogonal orientation of the aromatic rings of quercetin respect to the facet; this is consistent with the synthon analysis, where the hydrogen bond interaction between the hydroxyl groups of the quercetin and the carboxyl group of the quercetin and DMF drive the growth of this facet. The quercetin aromatic rings are instead exposed on facets {001} and {200}, forming an angle with the facet of 17.46° and 76.74°, respectively. The low inclination angle of the aromatic rings on the {001} facet enables the stacking interaction that characterizes the growth of this facet. Such interactions are not possible for the {200} facet due to the almost perpendicular orientation of the quercetin aromatic rings that promote hydrogen bonding.

This structural feature has a considerable impact on the rugosity of the two facets, with {200} showing a rougher surface while the {001} facet shows a smoother surface. In this way, the facet-dependent roughness is not treated as an isolated morphological descriptor but emerges as a direct consequence of how the molecular packing is oriented in relation to the surface plane.

Through the CSD-Particle suite it is also possible to determine the atomic composition for each facet, which is illustrated in Figure. S3 of Supporting Information [69]. The {1–10} facet exposes mostly sp^3 carbon from DMF (26.926) and lacks contribution from aromatic C atoms of quercetin, due to the orientation of these molecules. Facets {001} and {200} are instead dominated by the aromatic carbon atoms of quercetin, followed by sp^3 oxygen atoms of the same facets. The contribution of DMF atoms for these two facets is much lower than {1–10}, especially for the {001} facet. It is worth noticing the minimal contribution of the amide nitrogen from DMF across all facets.

IR spectroscopic characterization of powder and single crystal QDMF

The bulk ATR-FTIR spectra of QDMF and quercetin dihydrate (QDH) (the commercial form) powders are shown in Fig. 2. The characteristic

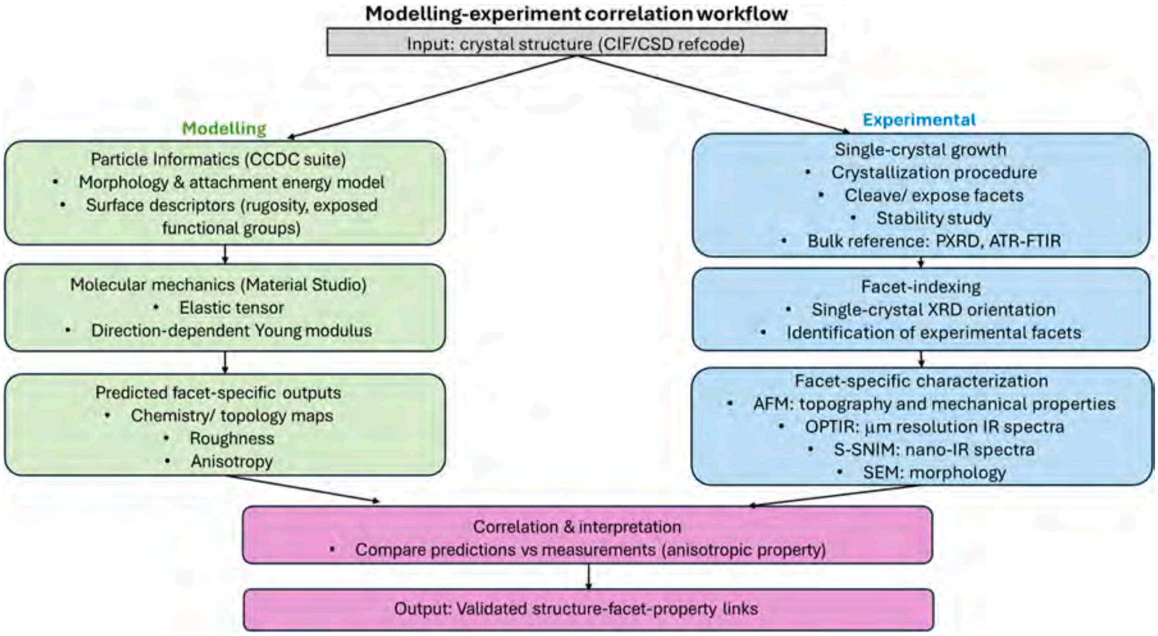

Chart. 1. Schematic representation of the workflow used in this paper for both modelling and experimental activities.

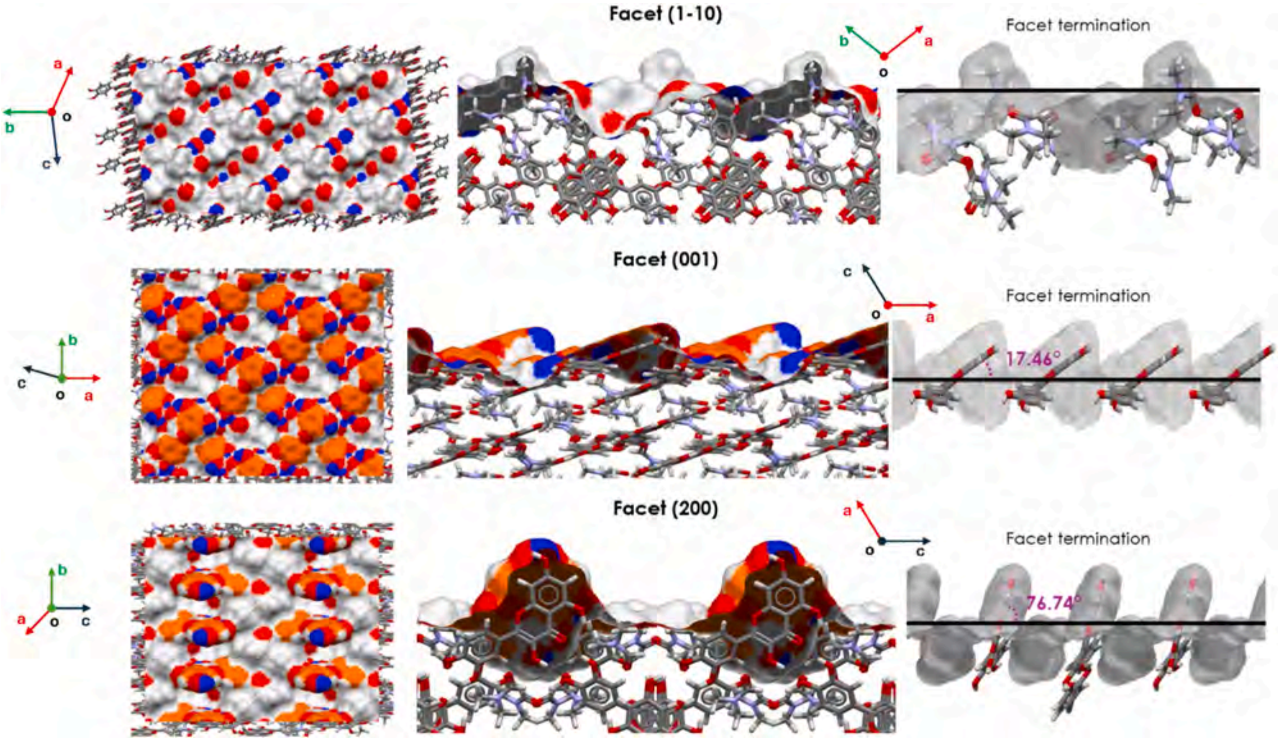

Fig.. 1. Surface topology of the main QDMF crystal facets. The three predominant facets, (1–10), (001), and (200) are shown. Surface colouring highlights chemical functionalities: hydrogen bonding donors (blue), hydrogen bonding acceptors (red), and aromatics (orange). Black lines represent the facet terminations. Crystallographic vectors are reported for the topology surfaces and facet terminations.

peaks for QDH are at 1014 cm^{-1} (out-of-plane C–H bending), 1257 cm^{-1} (the C–O stretching in the aryl ether), 1317 cm^{-1} (in-plane bending C–H), 1380 cm^{-1} (OH bending), and at 1662 cm^{-1} (C=O stretching) [78].

For QDMF it is also possible to identify characteristic peaks, which are associated with vibrational modes of both the DMF and quercetin molecules. C–H bending of DMF is detectable at 1063 and 1387 cm^{-1}, the asymmetric N–CH_3 stretching is evident at 1250 cm^{-1}, and the CN stretching is assigned at 1495 cm^{-1}. Additionally, QDMF presents two extra bands related to quercetin that are not visible in the QDH spectrum: the band at 1104 cm^{-1} is attributable to in-plane C–H and OH bending, while the band at 1369 cm^{-1} corresponds to OH bending [79–82].

Optical photothermal IR (OPTIR) spectroscopy was conducted on single crystals of QDMF exposing different facets by using the setup shown in Figure. S1 of the Supporting Information file. As this technique measures backscattered light, it could provide facet-specific

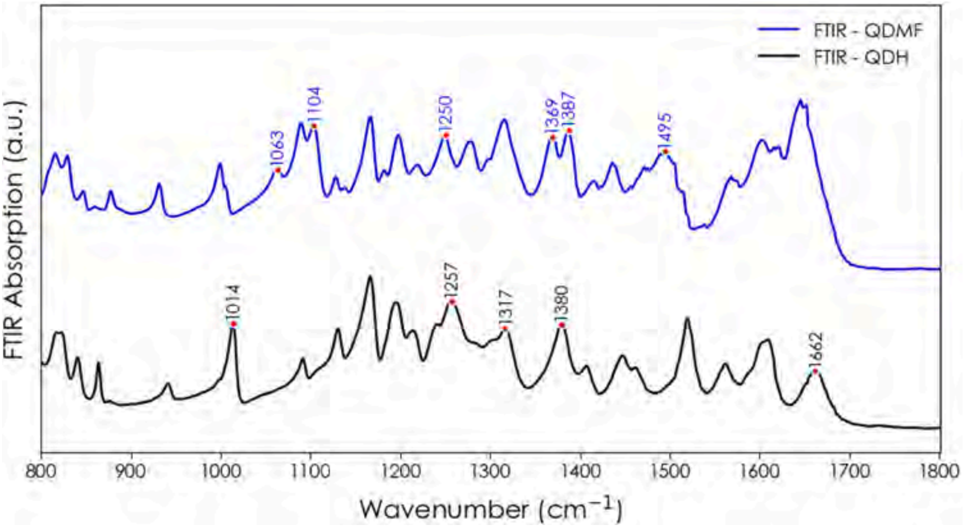

Fig.. 2. Comparison of ATR-FTIR spectra for QDMF and QDH. Spectra were acquired with a spectral resolution of 4 cm^{-1}, averaging 64 scans for each measurement.

information, with sub-micron spatial resolution, that could be linked with the computational analysis. The crystal facets were previously indexed through a single-crystal diffractometer by following the procedure described in the Materials and Methods. The same procedure was followed for the AFM and s-SNIM measurements reported in the following sections.

The crystallographic facets {1–10}, {001}, and {200} of QDMF were analysed after being freshly removed from solution. Multiple points on the same facet of different crystals were also examined at different focal planes to verify the consistency of the measurement. As shown in Figures S4 to S6 in Supporting Information, which present mean and standard deviation for all collected spectra of the same facet after normalization, significant differences in peak positions and relative intensities could be identified consistently among the three studied facets (Figures S7 and S8 in the Supporting Information). A thorough comparison can be made by looking at Fig. 3, which shows the averaged OPTIR spectra of different QDMF facets. The facet-dependent OPTIR spectra can be interpreted as proof and qualitative indication of packing anisotropy. It can be noticed that the bulk ATR-FTIR spectrum of Fig. 2 is characterized by a convolution of the peaks from all three facets of the QDMF crystals; this is particularly evident in the region between 1500 and 1800 cm^{-1}. In the OPTIR spectra, two major peaks at around 817 and 829 cm^{-1} can be observed for all three facets, with different relative intensities and slight shifts. The normalized intensity of these two peaks is much stronger for facets {200} and {1–10} compared to {001}. The characteristic vibration of this region is the out-of-plane C–H bending of aromatic compounds [78], which seems inhibited compared to other vibrational modes for the {001} facet. This is possibly related to the orientation of the aromatic rings of quercetin along this facet, as they lay relatively flat in order to favour the stacking interactions that characterize the growth of this facet [69].

The C–H groups of the quercetin aromatic rings are indeed orthogonal to the other two facets, possibly enabling stronger out-of-plane bending vibrations. On the other hand, facet {001} presents a peak of higher intensity than the other facets, at 1001 cm^{-1}, which is shifted to a higher frequency (1005 cm^{-1}) for the {1–10} facet. This peak can be associated with the in-plane vibrational mode of C–H [79], which is stronger for the flat quercetin molecules of facet {001} compared to the

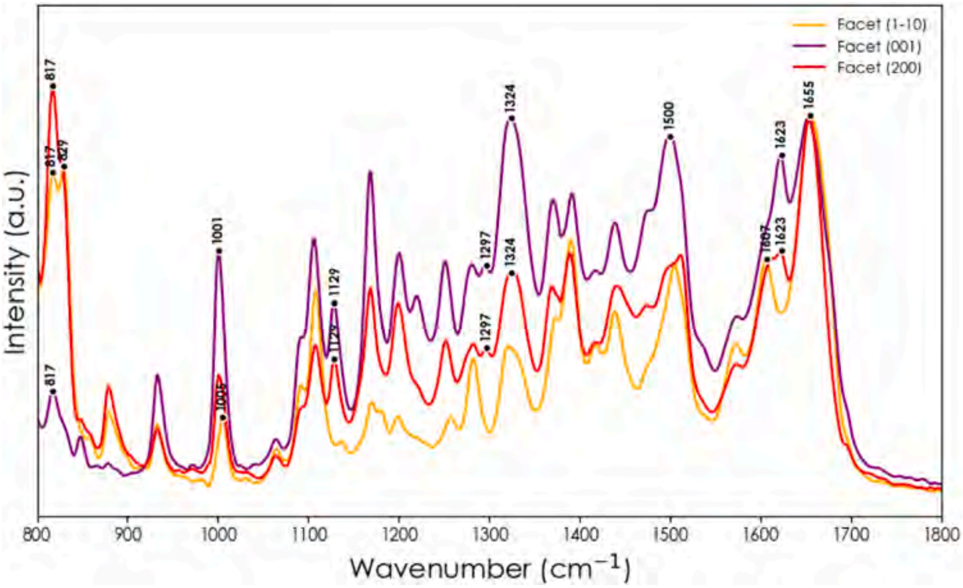

Fig.. 3. Normalized OPTIR spectra for each facet of the QDMF single crystal: {1–10}, {001}, and {200}. The spectra were normalized at the peak located at 1655 cm^{-1}.

{1–10} and {200}. Other major differences among facets are the higher intensity for the {001} of the peaks at 1324 cm^{-1} and 1500 cm^{-1} compared to the other two facets. The peak at 1324 cm^{-1} may be associated with in-plane C–H bending in aromatic hydrocarbons [79], and it is more intense for {001} and {200} facets, as it reflects the tilt angle of quercetin molecules for the facet termination. The band at 1500 cm^{-1} is assigned to the C=C stretching vibration [80–82], and it is more intense for the {001} facet due to the flat orientation of the quercetin molecules exposed on this facet.

The {001} and {200} facets present the same peaks at 1129 and 1297 cm^{-1}, not detectable on the {1–10}, corresponding to OH bending modes of the different hydroxyl groups present on the quercetin molecular backbone, or to C–OH deformation vibration of the same groups for the higher wavenumber peak [78]. In addition, in this case, the presence of these two peaks can be attributed to the orientation of the quercetin molecules shown in Fig. 1.

Finally, each spectrum shows two peaks at 1607 cm^{-1} and 1655 cm^{-1} that are assigned to C=C stretching and/or C=O stretching of the two different carboxyl groups [80–83], one from the quercetin and one from the DMF molecules. In the region from 1600 to 1700 are present three main peaks: 1607, 1623, and 1655. The first peak is present in each facet, while the 1623 peak is absent in the {1–10}. The last peak is shared by every facet.

The OPTIR signal intensity also depends on the orientation of molecular vibrational transition dipoles with respect to the electric-field vector of the IR excitation beam [84–87]. Consequently, the orientation of a given crystal facet relative to the IR beam polarization can significantly influence the relative peak heights observed in crystalline samples. This effect is particularly relevant for QDMF, in which the orientation of quercetin molecules varies markedly among different facets. As shown by the Particle Informatics analysis (Fig. 1), the aromatic rings of quercetin lie almost parallel to the {001} facet (tilt angle ~17°), whereas they are strongly titled on the {200} facet (~77°) and nearly perpendicular on the {1–10}. Because the transition dipoles associated with aromatic C—H bending, C=C stretching, and C—H in-plane modes are oriented within or normal to the aromatic ring planes, their coupling to the polarized IR field varies from facet to facet. Therefore, the facet-dependent differences in the relative intensities of the OPTIR bands observed in Fig. 3 do not arise solely from differences in exposed functional groups, but also from the orientation of molecular bonds with respect to the polarization of the incident electric field.

Scattering-type scanning near-field infrared microscopy (s-SNIM)

s-SNIM characterization was carried out on the {1–10} and {001} QDMF facets at room environmental conditions. Although sample instability, which was caused mainly by desolvation, posed challenges during measurement, it was still possible to compare the spectral features across different facets. Notably, desolvation led to the formation of specific structural changes (discussed in the following section), and it was evident both on s-SNIM and by optical microscopy through a surface colour shift from dark to bright yellow, allowing us to limit the investigation to non-degraded regions.

Fig. 4 presents the results obtained for the measurement of a fresh {1–10} facet. Fig. 4a displays the topography of the QDMF {1–10} facet, showing height variations in the range of approximately 0–40 nm. Infrared spectra were collected in the 1100–1800 cm^{-1} range, as presented in Fig. 4b

Compared to OPTIR spectra, s-SNIM data are characterized by a lower signal-to-noise ratio, reflecting the considerably higher spatial resolution of the system. In fact, the signal is acquired from a spot of about 20 × 20 nm^2, resulting in high sensitivity on the local nanometric features. From the data, it is still possible to identify the same characteristic peaks, such as C–O stretching vibrations observed at 1171 and 1208 cm^{-1}. Prominent peaks assigned to OH bending and aromatic C–H vibrations are visible at 1326, 1382 and 1574 cm^{-1}. DMF signature bands are identified at around 1439 and 1506 cm^{-1}, corresponding to asymmetric bending (CH_3)–N and stretching (CN) modes [80–83], respectively. A band at around 1253 cm^{-1}, attributed to asymmetric stretching (N–CH_3) of DMF is also evident.

The spectral differences among the different points of the same facet are minimal and suggest minor local variations in solvent retention or molecular packing, confirming the high crystalline homogeneity of different facets. This is consistent with the topographic height difference (~40 nm) being lower than the typical near-field signal subsurface penetration depth ≤ ~100 nm [88]. Similar spectra were obtained on the same facet of a different QDMF crystal as reported in Figure. S9 of Supporting Information, showing the consistency of this type of measurement for this facet.

Facet {001} was also analysed with s-SNIM, and the results are reported in Fig. 5. Cleaved facet {001} is significantly rougher than the {1–10} one, as shown in the topography of Fig. 5a.

The higher roughness of cleaved {001} can also be explained in terms of its anisotropic packing motif (it is worth noticing that the

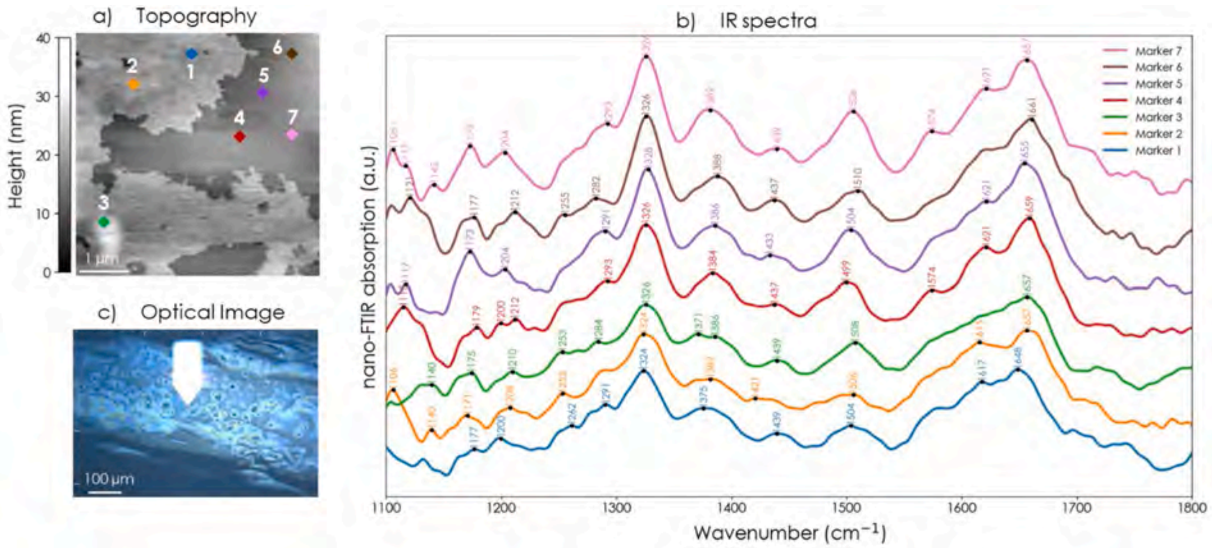

Fig.. 4. s-SNIM analysis on QDMF {1–10} facet. (a) AFM height image of the QDMF-solvated sample over a 5 × 5 μm^2 area. (b) Single-point IR spectra at seven selected locations corresponding to different topographic heights, reported in (a). (c) Microscopic image of the crystal facet showing the position of the cantilever.

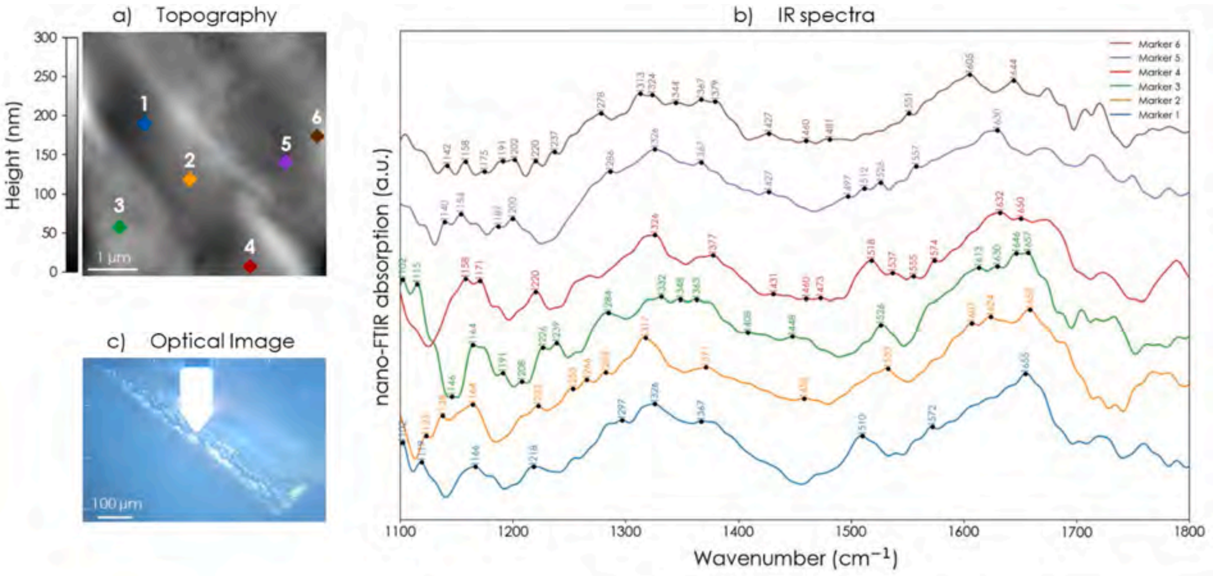

Fig.. 5. s-SNIM analysis on QDMF {001} facet. (a) AFM height image of the QDMF-solvated sample over a 5 × 5 µm^2 area. (b) Single-point IR spectra at six selected locations corresponding to different topographic heights, reported in (a). (c) Microscopic image of the crystal facet showing the position of the cantilever.

{1–10} was not cleaved before measurement). Because the growth of the {001} facet is characterized by offset stacking interactions between quercetin molecules, cleavage may preferentially occur through disruption/slippage of stacked layers, producing nanoscale height variations. The higher roughness also explains why single-point IR spectra are noisier, less defined, and less consistent compared to the {1–10} facet. Nevertheless, we can still observe a difference in the appearance of the spectra compared to the other measured facet. For example, the presence of the peak at around 1220 cm^{-1} only for facet {001}, which can also be observed in Fig. 3, and the higher intensity of peaks in the region 1150–1250 cm^{-1} for the {001} facet compared to the {1–10}. Other differences can be found in the region 1600 to 1800 cm^{-1} where facet {001} presents a characteristic peak at around 1630 cm^{-1}, while the same peak is shifted to 1620 cm^{-1} for the other facet. These results are also consistent with the OPTIR data and a summary table with peak assignment and facet-specific chemical interpretation is reported in the Supporting Information (Table S2).

Overall, noise in the relative peak-height ratios in OPTIR/s-SNIM may be related to polarization–orientation contributions; in our dataset this is most evident for s-SNIM (tip-antenna near-field polarization selectivity), whereas OPTIR acquired under a fixed configuration shows comparatively more uniform spectra.

Thermodynamic instability and facet-specific surface changes

QDMF facets, particularly the {001} one, undergo significant morphological changes over time due to desolvation phenomena. After 40 min, the formation of channel-like features on this facet becomes evident, as detected by both s-SNIM (Fig. 6, in Figures S9 to S12 of Supporting Information) and AFM (Fig. 7).

The desolvation process leads to the release of DMF molecules from the crystal lattice, triggering a structural reorganization within the bulk and surface, which was studied in more detail in our previous work [69]. In the AFM topography shown in Fig. 7a, three distinct surface regions are identified: a channel region (marker 1), a rough region (marker 2), and a smooth region (marker 3). These morphological features correlate directly with the chemical signatures observed in the corresponding s-SNIM spectra of Fig. 6b Comparison with the average spectrum for the solvated QDMF show that, in all three points, the characteristic DMF absorption at 1506 cm^{-1} is weaker, indicating that the solvent has left the crystal lattice. Additionally, shifts are observed for bands associated with several quercetin molecular vibrations: the C–H bending at 1326 cm^{-1} and the OH bending band at 1382 cm^{-1}. The presence of aromatic C=C stretching bands at 1514 cm^{-1} and 1611 cm^{-1} in marker 1, suggests a more ordered and less perturbed molecular arrangement within the

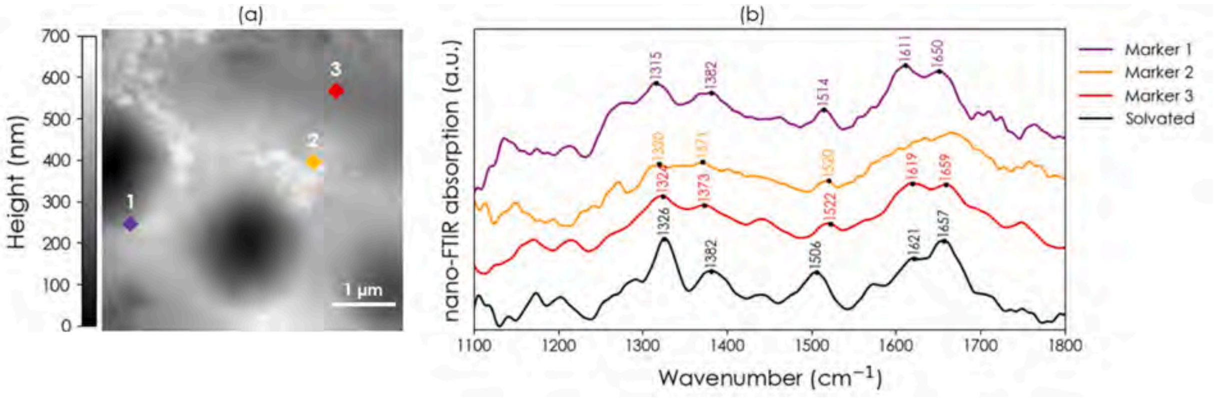

Fig.. 6. s-SNIM analysis on the QDMF {001} facet after the desolvation process. (a) AFM height map over a 5 × 5 µm^2 area. (b) Single-point s-SNIM spectra collected at three different regions of the {001} facet: channel region (marker 1, purple), rough region (marker 2, orange), and smooth region (marker 3, red). For comparison, the spectrum of the solvated compound on the {1–10} facet (solvated, black) is also shown.

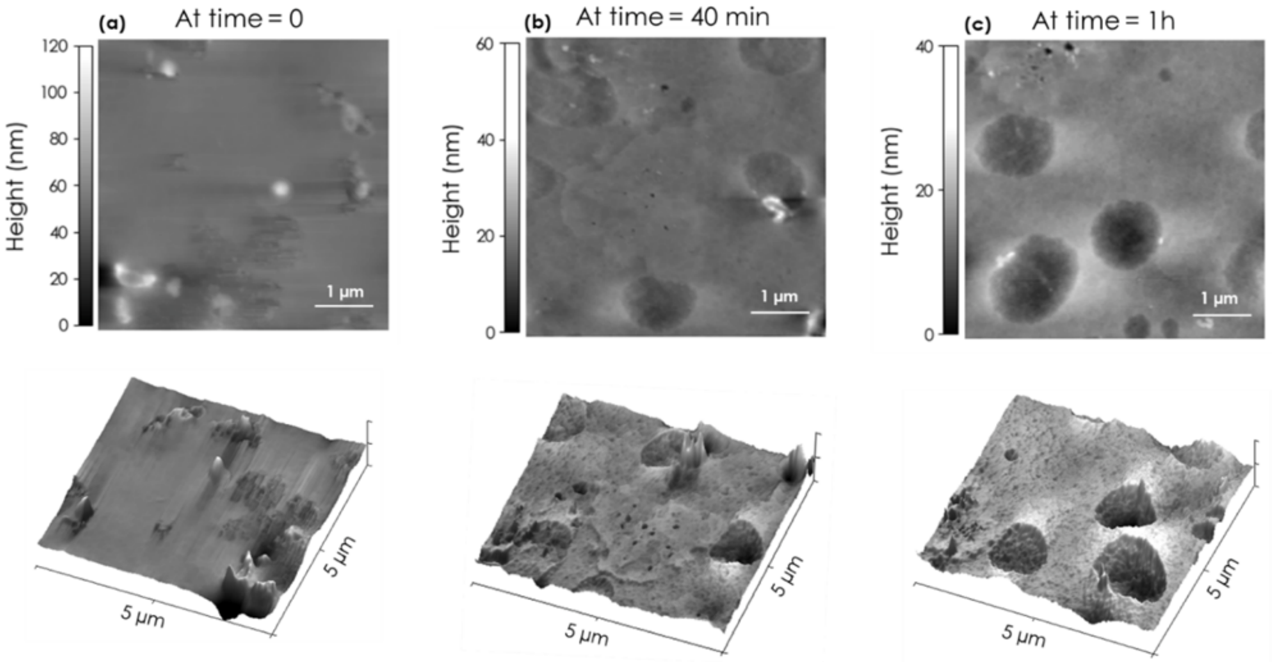

Fig.. 7. Temporal evolution of the QDMF crystal surface during de-solvation, monitored by AFM in tapping mode. (a) Immediately after removal from DMF, height scale: 0–120 nm. (b) After 40 min at room temperature, height scale: 0–60 nm. (c) After 1 hour at room temperature, height scale: 0–40 nm. In each panel, the upper image is the top-view height map, and the lower image is the corresponding 3D rendering, highlighting the progressive formation and deepening of channel-like features.

channel region compared to the other two points analysed. This indicates the rearrangement of the crystal structure upon desolvation, in agreement with previous measurements [69]. In the points indicated by markers 2 and 3, the aromatic modes are shifted toward higher frequencies, implying changes in molecular interactions and packing density. The spectral broadening and loss of defined peaks beyond 1520 cm^{-1} observed at marker 2 indicate a less homogeneous structure, likely caused by the ongoing recrystallization process. This interpretation is further supported by the disappearance of the C=O stretching band at 1650 cm^{-1} in marker 2, suggesting partial amorphization of the material in this region [83].

The s-SNIM analysis highlights that, while desolvation promotes channel formation and modifies the surface chemistry, these effects are spatially heterogeneous. Different regions on the {001} facet and different QDMF facets evolve at varying rates, depending on local factors such as the initial distribution of solvent molecules, crystallographic orientation [58], and the presence of defects on the surface.

Fig. 7 shows more details of the desolvation process, as captured by tapping-mode AFM. In the first 40 min, a pronounced decrease in maximum surface height is accompanied by the emergence of channel-like depressions aligned perpendicularly to the {1–10} facet. These surface features reflect rapid DMF loss and structural rearrangements within the crystal. After 40 min, the deepening and lateral propagation of channels slowed markedly, indicating depletion of the readily accessible solvent molecules and a shift to more gradual lattice-relaxation and molecular reorganization processes. While the

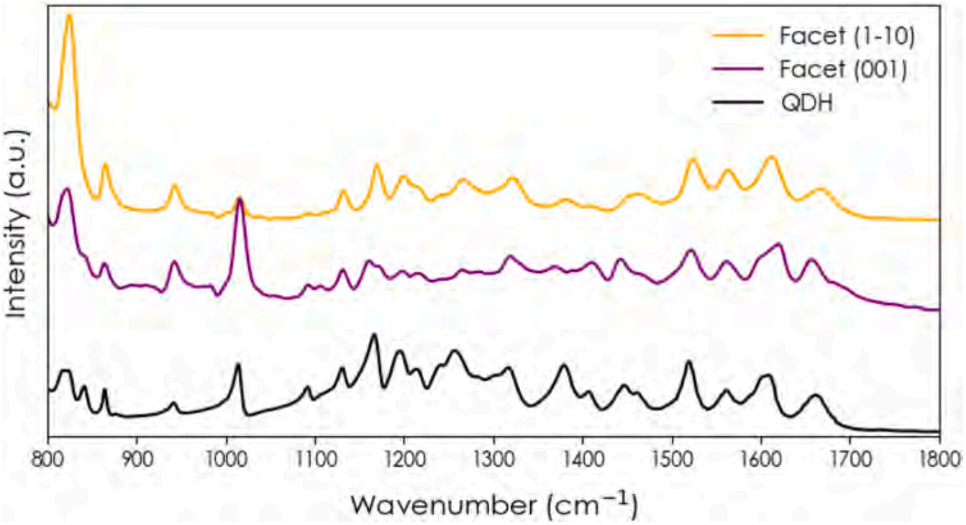

Fig.. 8. OPTIR spectra collected from the {1–10} and {001} facets of QDMF after 24 h of air exposure, compared with the spectrum of QDH. All the spectra were normalized with the peak of 1609 cm^{-1}.

quantitative information is fully contained in the 2D height maps, the 3D renderings (Fig. 7) provide complementary visualization of the depth and orientation of the channel-like depressions. This additional view facilitates interpretation of how desolvation features evolve and propagate along crystallographic directions.

Fig. 8 displays the OPTIR spectra collected from the {1–10} and {001} facets of QDMF crystals after 24 h of air exposure, compared with the spectrum of bulk quercetin dihydrate, QDH. All spectra were normalized in respect to the peak at 1609 cm^{-1} to allow direct comparison. Although all spectra indicate the same crystal structure, significant spectral differences can be observed between the two crystal facets and the bulk material. The {1–10} facet exhibits broader and more intense absorption features in the 1200–1700 cm^{-1} region, particularly in the bands associated with C=O stretching and aromatic C=C vibrations. These features suggest increased exposure or rearrangement of surface functional groups, potentially driven by facet-specific desolvation or degradation processes upon exposure to air. In contrast, the {001} facet displays narrower, less intense bands, indicating a comparatively more stable or less reactive surface under the same conditions. The spectral variation with QDH confirms that the surface chemistry of QDMF differs significantly from its bulk hydrated counterpart Table 1.

Bi-modal atomic force microscopy (AFM)

To investigate the mechanical properties of different facets, we used AM-FM AFM techniques to achieve nanoscale resolution of surface elasticity. Fig. 9 shows AFM images of Young modulus and height maps for a 5 × 5 μm^2 area of the QDMF capping facet {001}. Results indicate that the {001} facet exhibits a comparatively soft surface with variations in height up to 300 nm with average Young modulus values between 1 and 5 GPa, reflecting mechanical softness and nanoscale heterogeneity of this facet. The elastic modulus (E; GPa) and topography is shown in Fig. 9. In this case, the 3D rendering in the SI (Figure. S13) provides a more intuitive visualization of how mechanical heterogeneity (E values) is distributed across surface features, complementing the 2D maps. Additional maps are reported in Figures S14 to S16 of Supporting Information and show consistency of the measurements for different crystals and/or regions of the same crystal. This relative softness is clear when compared to the lateral {200} facet, which shows values between 7 and 10 GPa (almost twice as stiff), and is also consistent with the lower end of the range typically reported for organic molecular crystals [89]. The mean value of the Young modulus was calculated from the AM-FM AFM experimental maps for both the analysed facets and was found to be 4.09 GPa for the {001} and 6.52 GPa for the {200}. This difference between the {001} and {200} facets highlight the anisotropic mechanical properties of QDMF crystals, and this is due to the directionality of the intermolecular interactions that characterize the QDMF structures. The experimental values were compared with molecular mechanics calculation performed with the Materials Studio suite. The full 6 × 6 elastic tensor, compliance matrix, and direction-dependent mechanical moduli are reported in the Supporting Information (in the Materials Studio Young Modulus calculation section). The elastic tensor extracted from the supercell shows a marked anisotropy along the Y direction, as shown in Table 2. In particular, the Young modulus along the *b* axis (normal to the {200}) is almost twice that along the *c* axis (normal to the {001}). This is in agreement with the experimental data, although the actual values in GPa are higher for the simulations (15.1 and 8.3 GPa versus the experimental values of 6.52 and 4.09 GPa). This difference in modulus provides a direct mechanical manifestation of packing anisotropy. The {200} facet is normal to directions where strong and directional hydrogen-bonding interactions dominate the lattice connectivity; under indentation, these interactions act as comparatively stiff links, yielding a higher Young's modulus value. In contrast, the {001} facet is normal to a packing motif dominated by offset π-stacking, which presents higher strain under loading in normal direction compared to the {200} facet. This is due to the fact that offset π-stacking interactions enable local shear/slip between stacked layers, resulting in a lower apparent modulus. Importantly, this interpretation is consistent with the molecular-mechanics elastic-tensor analysis: the calculated Young modulus along the direction normal to {200} is substantially higher than that normal to {001}, capturing the same anisotropic trend observed experimentally (even if absolute values differ due to model assumptions such as ideal-crystal and the absence of defects, solvent dynamics, and near-surface effects). Considered together, the presented data support a coherent structure–property relationship, in which facet-specific intermolecular interaction topology governs both surface mechanics and topography.

Additionally, it can be noticed that the two analysed facets present different topographical textures, with the {200} facet being less homogeneous than the {001}. This may be due to the presence of residual solvent on the surface, as this facet was not pre-treated or cleaved before measurement. Our procedure relies on an accurate selection of the proper indentation regime to establish a defined nanomechanical contact. As shown in Figure. S17 in the SI, deeper indentation increases the contact area and radius, producing stable modulus values representative of the mechanical properties of the sample. Furthermore, to confirm the mapping of the capping {001} and lateral {200} facets by AFM, SEM images were acquired, as shown in Fig. 9c and Fig. 10c.

Conclusions

In this work, we establish a multi-technique framework that integrates Particle Informatics with facet-specific spectroscopy and nanomechanical mapping to obtain a comprehensive understanding of facet-dependent surface properties in QDMF. Computational tools were used to predict facet-specific chemistry, chemical nature, mechanical strength, and to relate them to the crystal structure. Computational results were validated using an unprecedented set of facet-specific measurements, including s-SNIM, OPTIR, and mechanical characterization by AFM, complemented by X-ray diffraction indexing. These measurements indicated significant differences among the experimental QDMF facets ({1–10}, {001}, and {200}), correlating their spectroscopic signatures and mechanical properties with simulated surface features. This

Table 1
Summary table mapping each method.

Techniques	Type	Main information provided	Why used/Facet-specific relevance
ATR-FTIR	Bulk	Average chemical composition and vibrational fingerprint	Provides reference bulk spectra; no sample preparation needed and high signal-to-noise ratio
XRD	Bulk and facet indexing	Crystal structure determination, and reciprocal-lattice orientation	Indexing of QDMF experimental facets ({1–10}, {001}, {200})
Particle Informatics	Facet-specific	Analyse intermolecular interactions, calculate and inspect the particle morphology, evaluate surface energy and surface interactions	Determination of facet-specific chemistry directly from crystal structure; guides and rationalizes analytical experiments
OPTIR	Facet-specific	Facet-specific vibrational fingerprint	Easy sample preparation, high spatial resolution, fast acquisition and insensitive to size and shape scattering artifacts
s-SNIM	Facet-specific	Nanoscale chemical and structural heterogeneity on single facets	Imaging information and AFM-high resolution
AM-FM AFM	Facet-specific	Surface topography and mechanical properties (Young Modulus)	Fast and high-resolution mapping of elastic properties

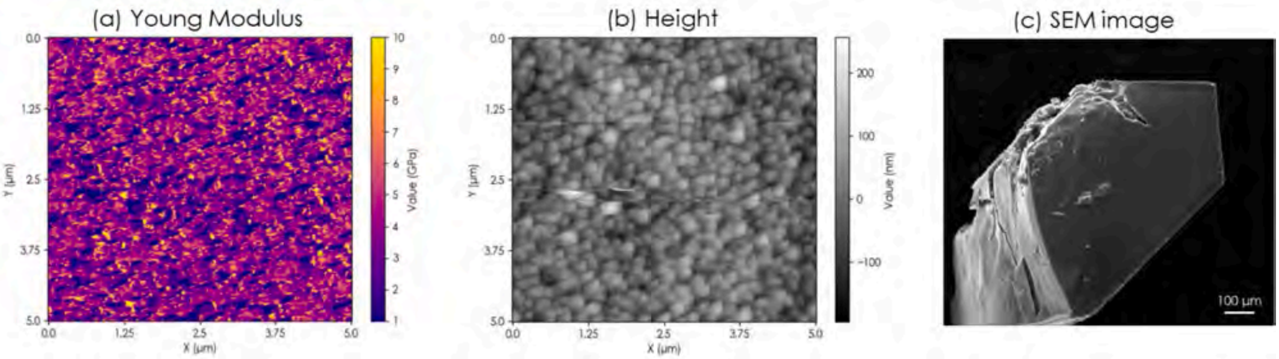

Fig.. 9. AFM images of QDMF capping facet {001}. (a) Young modulus (E; GPa) image and (b) height image for 5 × 5 μm^2 area, and (c) SEM image.

Table 2
Directional Young moduli constants derived from the elastic tensor of the 4 × 4 × 4 supercell.

Miller family	Experimental elastic modulus (GPa)	Calculated elastic modulus (GPa)
{010}	n/a	7.86 ± 0.15
{200}	6.52 ± 0.10	15.12 ± 0.16
{001}	4.09 ± 0.02	8.26 ± 0.09

agreement shows the potential of Particle Informatics tools for the design and characterization of crystalline particles with tailored surface properties.

Computational analysis highlighted how the orientation of quercetin molecules dictates the dominant interactions responsible for crystal growth but also for facet-specific mechanical and chemical properties. The {001} facet is primarily growing via stacking between quercetin aromatic rings, while the {1–10} and {200} facets are dominated by hydrogen bonding involving quercetin and DMF molecules. These predicted differences in intermolecular interactions are directly reflected in the experimental data. OPTIR spectroscopy shows stronger in-plane C–H and C=C vibrations on the {001} facet, consistent with the flatter orientation of the quercetin aromatic rings. By contrast, out-of-plane bending modes were more prominent on the {1–10} and {200} facets. s-SNIM provides a complementary nanoscale validation, by enabling the chemical mapping of individual facets, thereby bridging molecular level predictions and macroscopic facet measurements. Finally, mechanical property mapping via AM-FM AFM revealed differences in Young modulus between facets. s-SNIM spectroscopy further enabled spatially resolved chemical mapping of individual facets. Mechanical property mapping via AM-FM AFM revealed differences in Young modulus between facets. The {001} facet exhibited lower modulus values (1–5 GPa), indicative of mechanical softness due to the weaker nature of the offset stacking interactions characterizing the growth of this facet, whereas the H-bond growing {200} facet showed significantly higher values (7–10 GPa), pointing to a stiffer, more rigid mechanical behaviour. Overall, through careful experimental validation this study demonstrates how Particle Informatics tools can be effectively used to determine the role of crystal structure in dictating facet-specific structural, chemical, and mechanical properties of organic molecular crystals. Additionally, we demonstrated how computational tools can help estimate surface properties, particularly facet-specific anisotropy, reducing the time needed for high-resolution, time-consuming surface characterization techniques, which can be used for final validation. While QDMF was selected as model organic compound because it exposes, large, indexable facets, the proposed workflow can be broadly applied to other organic crystalline materials whose performance is influenced by surface anisotropy. In particular, facet-specific computational analyses and multi-technique experimental characterization can be useful tools for the study of pharmaceutical and fine-chemical solids (polymorphs, salts, cocrystal, hydrates/solvates), where wettability, dissolution, adhesion to excipients, flowability, compaction and humidity-driven transformations are often dependent on facet-specific properties [90–94]. A better understanding of the link between crystal structure and these properties is crucial to ensure smooth particle manufacturing and controlled release behaviour after administration. Beyond formulation science, the same approach could be relevant to functional organic crystals and organic semiconductors, where the exposed stacking or H-bond motifs at specific facets control interfacial charge injection [95], optical anisotropy and stability [96], as well as to porous crystalline frameworks in which facet terminations determine adsorption, catalytic activity, and chemical stability [97,98]. Overall, combining Particle Informatics with multiple analytical techniques provides a general route to link crystal packing to surface-controlled properties, enabling morphology-by-design strategies across multiple application domains.

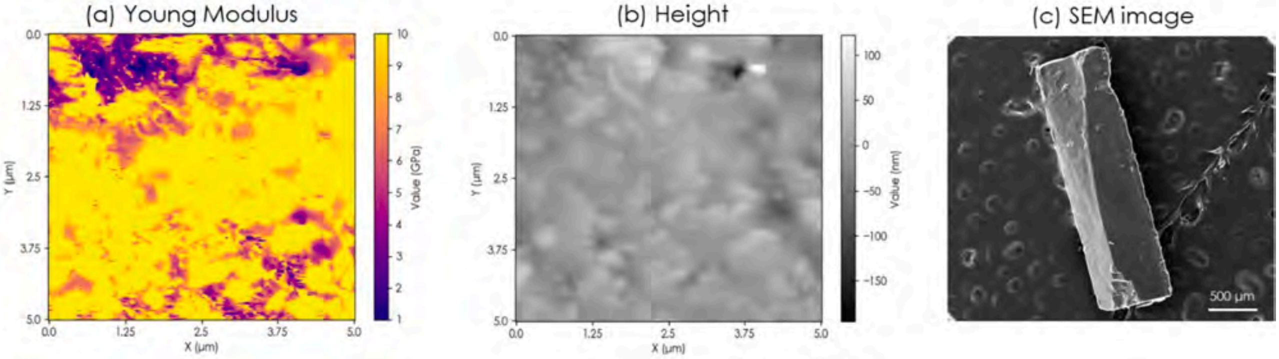

Fig.. 10. AFM images of QDMF lateral facet {200}. (a) Young modulus image and (b) height image for 5 × 5 μm^2 area, and (c) SEM image.

Supporting information

The Supporting Information is available free of charge.

The Supporting Information includes OPTIR technique diagram, experimental morphology and surface chemistry of QDMF, O-PTIR additional spectra, topography, *s*-SNIM spectra and optical image of QDMF facets, AM-FM measurement of different facets, Materials Studio Young modulus calculation parameters and output.

Data and metadata will be made open access in public repositories (Zenodo).

CRediT authorship contribution statement

Emilia Prandini: Writing – review & editing, Writing – original draft, Validation, Investigation, Formal analysis, Data curation. **Bruno Torre:** Writing – review & editing, Methodology, Investigation. **Emanuele Bosurgi:** Investigation. **Andrew G.P. Maloney:** Writing – review & editing, Supervision, Resources, Methodology, Funding acquisition. **Chiaramaria Stani:** Writing – review & editing, Methodology, Investigation. **Giovanni Birarda:** Writing – review & editing, Methodology, Investigation. **Lisa Vaccari:** Resources. **Enzo Mario Di Fabrizio:** Writing – review & editing, Supervision, Resources, Methodology. **Emmanuele Parisi:** Writing – review & editing, Writing – original draft, Validation, Supervision, Methodology, Investigation. **Elena Simone:** Writing – review & editing, Writing – original draft, Supervision, Resources, Methodology, Investigation, Funding acquisition, Conceptualization.

Declaration of competing interest

The authors declare that they have no known competing financial interests or personal relationships that could have appeared to influence the work reported in this paper.

Acknowledgements

This project has received funding from the European Research Council (ERC) under the European Union's Horizon 2020 research and innovation program (grant agreement no. 949229, awarded to the corresponding author). The authors are grateful to the Cambridge Crystallographic Data Centre for co-funding the PhD scholarship of Emilia Prandini. We acknowledge Elettra Sincrotrone Trieste for beamtime on the SISSI-Bio beamline (proposal number 20240128). We thank Federico Gorrini and Giulio Teti for the insightful discussions.

Supplementary materials

Supplementary material associated with this article can be found, in the online version, at doi:10.1016/j.apsadv.2026.100939.

Data availability

Data are available on Zenodo at the following doi:10.5281/zenodo.18338368.

References

[1] R.E. Newnham, Properties of Materials: Anisotropy, Symmetry, Structure, Oxford University Press, Oxford, 2020, https://doi.org/10.1093/oso/9780198520757.001.0001.

[2] I. Rosbottom, K.J. Roberts, R. Docherty, The solid state, surface and morphological properties of p-aminobenzoic acid in terms of the strength and directionality of its intermolecular synthons, Cryst. Eng. Comm. 17 (2015) 5768–5788, https://doi.org/10.1039/c5ce00302d.

[3] M.J. Turner, S.P. Thomas, M.W. Shi, D. Jayatilaka, M.A. Spackman, Energy frameworks: insights into interaction anisotropy and the mechanical properties of molecular crystals, Chem. Commun. 51 (2015) 3735–3738, https://doi.org/10.1039/c4cc09074h.

[4] P. Klitou, I. Rosbottom, V. Karde, J.Y.Y. Heng, E. Simone, Relating crystal structure to surface properties: a study on quercetin solid forms, Cryst. Growth Des. 22 (2022) 6103–6113, https://doi.org/10.1021/acs.cgd.2c00707.

[5] P. Klitou, I. Rosbottom, E. Simone, Synthonic modeling of quercetin and its hydrates: explaining crystallization behavior in terms of molecular conformation and crystal packing, Cryst. Growth Des. 19 (2019) 4774–4783, https://doi.org/10.1021/acs.cgd.9b00650.

[6] B.M.C.T. Peluzo, R. Meena, L. Catalano, G. Schweicher, M.T. Ruggiero, Exploring the interplay of lattice dynamics and charge transport in organic semiconductors: progress toward rational phonon engineering, Angew. Chem. Int. Ed. 64 (2025) e202507566, https://doi.org/10.1002/anie.202507566.

[7] K. Li, P. Yang, D. Xue, Anisotropic hardness prediction of crystalline hard materials from the electronegativity, Acta Mater 60 (2012) 35–42, https://doi.org/10.1016/j.actamat.2011.09.011.

[8] E. Ahmed, D.P. Karothu, P. Naumov, Crystal adaptronics: mechanically reconfigurable elastic and superelastic molecular crystals, Angew. Chem. Int. Ed. 57 (2018) 8837–8846, https://doi.org/10.1002/anie.201800137.

[9] G. Kaupp, J. Schmeyers, U.D. Hangen, Anisotropic molecular movements in organic crystals by mechanical stress, J. Phys. Org. Chem. 15 (2002) 307–313, https://doi.org/10.1002/poc.487.

[10] C.A. Brookes, J.B. O'Neill, B.A.W. Redfern, D. Tabor, Anisotropy in the hardness of single crystals, Proc. R. Soc. Lond. A 322 (1971) 73–88, https://doi.org/10.1098/rspa.1971.0055.

[11] S. Bhunia, S.K. Karan, R. Chowdhury, I. Ghosh, S. Saha, K. Das, A. Mondal, A. Nanda, B.B. Khatua, C.M. Reddy, Mechanically flexible piezoelectric organic single crystals for electrical energy harvesting, Chem 10 (2024) 1741–1754, https://doi.org/10.1016/j.chempr.2024.01.019.

[12] B. Jing, W. Kuang, J. Li, Y. Zhang, S. Wu, L. Li, P. Naumov, J. Gong, Colossal thermal expansion and continuous rolling locomotion of a robust flexible molecular single crystal, J. Am. Chem. Soc. 147 (2025) 22488–22497, https://doi.org/10.1021/jacs.5c02006.

[13] A. Yao, H. Xu, K. Shao, C. Sun, C. Qin, X. Wang, Z. Su, Guest-induced structural transformation of single-crystal 3D covalent organic framework at room and high temperatures, Nat. Commun. 16 (2025) 1385, https://doi.org/10.1038/s41467-025-56750-9.

[14] L. Catalano, D.P. Karothu, S. Schramm, E. Ahmed, R. Rezgui, T.J. Barber, A. Famulari, P. Naumov, Dual-mode light transduction through a plastically bendable organic crystal as an optical waveguide, Angew. Chem. Int. *Ed* 57 (2018) 17254.

[15] I. Azuri, E. Meirzadeh, D. Ehre, S.R. Cohen, A.M. Rappe, M. Lahav, I. Lubomirsky, L. Kronik, Unusually large Young's moduli of amino acid molecular crystals, Angew. Chem. Int. Ed. 54 (2015) 13566–13570, https://doi.org/10.1002/anie.201505813.

[16] S. SeethaLekshmi, M.S.R.N. Kiran, U. Ramamurty, S. Varughese, Molecular basis for the mechanical response of sulfa drug crystals, Chem. Eur. J. 25 (2019) 526, https://doi.org/10.1002/chem.201803987.

[17] M.K. Panda, R. Centore, M. Causà, A. Tuzi, F. Borbone, P. Naumov, Strong and anomalous thermal expansion precedes the thermosalient effect in dynamic molecular crystals, Sci. Rep. 6 (2016) 29610, https://doi.org/10.1038/srep29610.

[18] E. Parisi, E. Santagata, P. Kula, J. Herman, S. Gupta, E. Simone, S. Zarrella, T. M. Korter, R. Centore, Mechanical transitions in crystals: the low-temperature thermosalient transition of a mesogenic polyphenyl, J. Am. Chem. Soc. 147 (2025) 14731–14738, https://doi.org/10.1021/jacs.5c03448.

[19] C.M. Reddy, Plasticity enhancement in pharmaceutical drugs by water of crystallization: unusual slip planes, IUCrJ 6 (2019) 505–506, https://doi.org/10.1107/S205225251900890X.

[20] J.P. Yadav, R.N. Yadav, P. Sihota, H. Chen, C. Wang, C.C. Sun, N. Kumar, A. Bansal, S. Jain, Single-crystal plasticity defies bulk-phase mechanics in isoniazid cocrystals with analogous coformers, Cryst. Growth Des. 19 (2019) 4465–4475, https://doi.org/10.1021/acs.cgd.9b00247.

[21] J. Wen, T. Li, Z. Du, X. Wang, Y. Yang, M. Duan, J. Yang, H. Zhang, Y. Chen, Modulation of elastic perovskites for flexible photovoltaics, Nano Energy 142 (2025) 111267, https://doi.org/10.1016/j.nanoen.2025.111267.

[22] W.A. Wooster, Physical properties and atomic arrangements in crystals, Rep. Prog. Phys. 16 (1953) 62, https://doi.org/10.1088/0034-4885/16/1/302.

[23] N. Kalita, P. Deka, I. Ghosh, K.J. Kalita, A. Gogoi, C.M. Reddy, R. Thakuria, Odd–even effect controls twist-elasticity of an organic fluorophore in cocrystals prepared using mechanochemistry, J. Mater. Chem. C 13 (2025) 10769–10779, https://doi.org/10.1039/D5TC00313J.

[24] W.B. Stoll, P.A. Banks, S.G. Dannenberg, R. Waterman, L. Catalano, M.T. Ruggiero, Interrogation of the intermolecular forces that drive bulk properties of molecular crystals with terahertz spectroscopy and density functional theory, Cryst. Growth Des. 25 (2025) 3697–3706, https://doi.org/10.1021/acs.cgd.5c00007.

[25] E.A. Verhaeg, H. Hoshina, J. Kikuchi, L. Catalano, M.T. Ruggiero, Solving the cellulose I polymorphic structural riddle: disorder in hydrogen bond networks activates diagnostic terahertz dynamics, J. Mater. Chem. C (2025), https://doi.org/10.1039/D5TC01544H.

[26] J.Y.Y. Heng, A. Bismarck, A.F. Lee, K. Wilson, D.R. Williams, Anisotropic surface energetics and wettability of macroscopic Form I paracetamol crystals, Langmuir 22 (2006) 2760–2769, https://doi.org/10.1021/la0532407.

[27] J.Y.Y. Heng, D.R. Williams, Wettability of paracetamol polymorphic forms I and II, Langmuir 22 (2006) 6905–6909, https://doi.org/10.1021/la060596p.

[28] T. Jain, S. Sheokand, S.R. Modi, B. Ugale, R.N. Yadav, N. Kumar, C.M. Nagaraja, A. K. Bansal, Effect of differential surface anisotropy on performance of two plate-shaped crystals of aspirin Form I, Eur. J. Pharm. Sci. 99 (2017) 318–327, https://doi.org/10.1016/j.ejps.2016.12.034.

[29] J.Y.Y. Heng, A. Bismarck, A.F. Lee, K. Wilson, D.R. Williams, Anisotropic surface chemistry of aspirin crystals, J. Pharm. Sci. 96 (2007) 2134–2144, https://doi.org/10.1002/jps.20841.

[30] R. Ho, M. Naderi, J.Y.Y. Heng, D.R. Williams, F. Thielmann, P. Bouza, A.R. Keith, G. Thiele, D.J. Burnett, Effect of milling on particle shape and surface energy heterogeneity of needle-shaped crystals, Pharm. Res. 29 (2012) 2806–2816, https://doi.org/10.1007/s11095-012-0842-1.

[31] P.P. Upadhyay, M.K. Mishra, U. Ramamurty, A.D. Bond, Mechanical anisotropy and tabletability of famotidine polymorphs, Cryst. Eng. Comm. 24 (2022) 1795–1802, https://doi.org/10.1039/D1CE01406D.

[32] S.R. Modi, A.K.R. Dantuluri, V. Puri, Y.B. Pawar, P. Nandekar, A.T. Sangamwar, S. R. Perumalla, C.C. Sun, A.K. Bansal, Impact of crystal habit on biopharmaceutical performance of celecoxib, Cryst. Growth Des. 13 (2013) 2824–2832, https://doi.org/10.1021/cg400140a.

[33] A.L. Briseno, S.C.B. Mannsfeld, M.M. Ling, S. Liu, R.J. Tseng, C. Reese, M. E. Roberts, Y. Yang, F. Wudl, Z. Bao, Patterning organic single-crystal transistor arrays, Nature 444 (2006) 913–917, https://doi.org/10.1038/nature05427.

[34] V.C. Sundar, J. Zaumseil, V. Podzorov, E. Menard, R.L. Willett, T. Someya, M. E. Gershenson, J.A. Rogers, Elastomeric transistor stamps: reversible probing of charge transport in organic crystals, Science 303 (2004) 1644–1646, https://doi.org/10.1126/science.1094196.

[35] Q. Li, Y. Xu, Z. Yao, J. Kang, X. Liu, C. Wolverton, M.C. Hersam, J. Wu, V.P. Dravid, Revealing the effects of electrode crystallographic orientation on battery electrochemistry via the anisotropic lithiation and sodiation of ReS_2, ACS Nano 12 (2018) 7875–7882, https://doi.org/10.1021/acsnano.8b02203.

[36] A. Jain, H.S. Shah, P.R. Johnson, A.S. Narang, K.R. Morris, R.V. Haware, Crystal anisotropy explains structure–mechanics impact on tableting performance of flufenamic acid polymorphs, Eur. J. Pharm. Biopharm. 132 (2018) 83–92, https://doi.org/10.1016/j.ejpb.2018.09.006.

[37] T. Li, A. Mattei, Pharmaceutical Crystals: Science and Engineering, John Wiley & Sons, 2018, https://doi.org/10.1002/9781119046233.

[38] M.D. Ward, Bulk crystals to surfaces: combining X-ray diffraction and atomic force microscopy to probe the structure and formation of crystal interfaces, Chem. Rev. 101 (2001) 1697–1726, https://doi.org/10.1021/cr000020j.

[39] P. Zhang, Z. Bi, H. Yu, R. Wang, G. Sun, S. Zhang, Effect of particle surface roughness on the flowability and spreadability of Haynes 230 powder during laser powder bed fusion process, J. Mater. Res. Technol. 26 (2023) 4444–4454, https://doi.org/10.1016/j.jmrt.2023.08.173.

[40] S.E. Brika, M. Letteneur, C.A. Dion, V. Brailovski, Influence of particle morphology and size distribution on the powder flowability and laser powder bed fusion manufacturability of Ti-6Al-4V alloy, Addit. Manuf. 31 (2020) 100929, https://doi.org/10.1016/j.addma.2019.100929.

[41] T. Chowdhury, F. Mujid, Z. Naqvi, A. Ray, C. Liang, D.A. Muller, N.P. Guisinger, J. Park, Spectra-orthogonal optical anisotropy in wafer-scale molecular crystal monolayers, Nano Lett 25 (2025) 5852–5859, https://doi.org/10.1021/acs.nanolett.5c00731.

[42] I. Bade, V. Karde, L. Schenck, M. Solomos, M. Figus, C. Chen, S. Axnanda, J.Y. Y. Heng, Process-induced crystal surface anisotropy and the impact on the powder properties of odanacatib, Pharmaceutics 16 (2024) 883, https://doi.org/10.3390/pharmaceutics16070883.

[43] M. Najib, R.B. Hammond, T. Mahmud, T. Izumi, Impact of inequivalent wetting on the face-specific dissolution rates for single faceted crystals predicted from solid-state binding energies, Cryst. Growth Des. 24 (2024) 4894–4905, https://doi.org/10.1021/acs.cgd.2c00043.

[44] J.V. Davis, H. Singh, J.D. Moore, C.F.A. Negre, R. Perriot, Solvent effects on the crystal morphology of pentaerythritol tetranitrate (PETN), Cryst. Growth Des. 25 (2025) 1940–1948, https://doi.org/10.1021/acs.cgd.5c00146.

[45] E. Simone, A.R. Klapwijik, C.C. Wilson, Z.K. Nagy, Investigation of the evolution of crystal size and shape during temperature cycling and in the presence of a polymeric additive using combined process analytical technologies, Cryst. Growth Des. 17 (2017) 1695–1706, https://doi.org/10.1021/acs.cgd.6b01683.

[46] H. Eisenschmidt, N. Bajcinca, K. Sundmacher, Optimal control of crystal shapes in batch crystallization experiments by growth–dissolution cycles, Cryst. Growth Des. 16 (2016) 3297–3306, https://doi.org/10.1021/acs.cgd.6b00288.

[47] D. Etit, I. Bade, C.T.T. Tan, J.Y.Y. Heng, Post-breakage crystal regeneration: multiple breakage sites, growth kinetics, and effects on mass production, Cryst. Growth Des. 25 (2025) 8073–8080, https://doi.org/10.1021/acs.cgd.5c00806.

[48] C.Y. Ma, K.J. Roberts, Morphological population balance modelling of the effect of crystallisation environment on the evolution of crystal size and shape of para-aminobenzoic acid, Comput. Chem. Eng. 126 (2019) 356–370, https://doi.org/10.1016/j.compchemeng.2019.04.019.

[49] A. Reinhold, H. Briesen, High dimensional population balances for the growth of faceted crystals: combining Monte Carlo integral estimates and the method of characteristics, Chem. Eng. Sci. 127 (2015) 220–229, https://doi.org/10.1016/j.ces.2015.01.035.

[50] T.H. Muster, C.A. Prestidge, Face specific surface properties of pharmaceutical crystals, J. Pharm. Sci. 91 (2002) 1432–1444, https://doi.org/10.1002/jps.10125.

[51] Y. Diao, A.S. Myerson, T.A. Hatton, B.L. Trout, Surface design for controlled crystallization: the role of surface chemistry and nanoscale pores in heterogeneous nucleation, Langmuir 27 (2011), https://doi.org/10.1021/la104351k, 5334–24.

[52] A.J. Page, R.P. Sear, Crystallization controlled by the geometry of a surface, J. Am. Chem. Soc. 131 (2009) 17550–17551, https://doi.org/10.1021/ja9085512.

[53] Y.H. Kiang, C.-Y. Yang, R.J. Staples, J. Jona, Crystal structure, crystal morphology, and surface properties of an investigational drug, Int. J. Pharm. 368 (2009) 76–82, https://doi.org/10.1016/j.ijpharm.2008.09.062.

[54] X. Cao, C. Sun, T.J. Thamann, A study of sulfamerazine single crystals using atomic force microscopy, transmission light microscopy, and Raman spectroscopy, J. Pharm. Sci. 94 (2005) 1881–1892, https://doi.org/10.1002/jps.20402.

[55] S. Kim, M.C. Marcano, U. Becker, Effects of hydroxyl and carboxyl functional groups on calcite surface wettability using atomic force microscopy and density functional theory, ACS Earth Space Chem 5 (2021) 2545–2554, https://doi.org/10.1021/acsearthspacechem.1c00240.

[56] R. Chai, Y. Liu, Q. Liu, J. Xin, Interaction mechanism of calcite and four representative organic molecules: experiments and DFT study, Colloids Surf. A Physicochem. Eng. Asp. 612 (2021) 125822, https://doi.org/10.1016/j.colsurfa.2020.125822.

[57] R. García, Interfacial liquid water on graphite, graphene, and 2D materials, ACS Nano 17 (2023) 51–69, https://doi.org/10.1021/acsnano.2c10215.

[58] D. Daniel, M. Vuckovac, M. Backholm, M. Latikka, R. Karyappa, X.Q. Koh, J.V. I. Timonen, N. Tomczak, R.H.A. Ras, Probing surface wetting across multiple force, length and time scales, Commun. Phys. 6 (2023) 152, https://doi.org/10.1038/s42005-023-01268-z.

[59] O.I. Oresegun, R.Z. Kabantiyok, E.D. Chinemerem, E.F. Oluwadarasimi, Md.S.Y. Z. Sparsha, U. Mohsin, A.C. Ikeji, M.I. Abdulrahman, M.C. Sekete, Advanced characterization techniques for organic and inorganic materials: emerging trends, innovations, and multidisciplinary applications, World J. Adv. Res. Rev. 26 (2025) 279–314, https://doi.org/10.30574/wjarr.2025.26.3.2188.

[60] W. Fu, W. Zhang, Hybrid AFM for nanoscale physicochemical characterization: recent development and emerging applications, Small 13 (2017) 1603525, https://doi.org/10.1002/smll.201603525.

[61] A. Dazzi, C.B. Prater, AFM-IR: technology and applications in nanoscale infrared spectroscopy and chemical imaging, Chem. Rev. 117 (2017) 5146–5173, https://doi.org/10.1021/acs.chemrev.6b00448.

[62] V.D. dos Santos, A.C. Hondl, V. Ramos-Garcia, J. Kuligowski, B. Lendl, G. Ramer, AFM-IR for nanoscale chemical characterization in life sciences: recent developments and future directions, ACS Meas. Sci. Au 3 (2023) 301–314, https://doi.org/10.1021/acsmeasuresciau.3c00010.

[63] F. Huth, A. Govyadinov, S. Amarie, W. Nuansing, F. Keilmann, R. Hillenbrand, Nano-FTIR absorption spectroscopy of molecular fingerprints at 20 nm spatial resolution, Nano Lett 12 (2012) 3973–3978, https://doi.org/10.1021/nl301159v.

[64] C.B. Prater, M. Kansiz, J.-X. Cheng, A tutorial on optical photothermal infrared (O-PTIR) microscopy, APL Photonics 9 (2024) 091101, https://doi.org/10.1063/5.0219983.

[65] L. Xiao, Z.D. Schultz, Spectroscopic imaging at the nanoscale: technologies and recent applications, Anal. Chem. 90 (2018) 440–458, https://doi.org/10.1021/acs.analchem.7b04151.

[66] M. Wagner, Q. Hu, S. Hu, C. Phillips, W. Wang, B. Pittenger, A. Fali, C. Li, J. Mathurin, A. Dazzi, C. Su, P. De Wolf, Force volume atomic force microscopy–infrared for simultaneous nanoscale chemical and mechanical spectromicroscopy, ACS Nano 19 (2025) 18791–18803, https://doi.org/10.1021/acsnano.5c04015.

[67] M. Kocun, A. Labuda, W. Meinhold, I. Revenko, R. Proksch, Fast, high-resolution, and wide modulus range nanomechanical mapping with bimodal tapping mode, ACS Nano 11 (2017) 10097–10105, https://doi.org/10.1021/acsnano.7b04530.

[68] M.F. Dupont, A. Elbourne, E. Mayes, K. Latham, Measuring the mechanical properties of flexible crystals using bi-modal atomic force microscopy, Phys. Chem. Chem. Phys. 21 (2019) 20219–20224, https://doi.org/10.1039/C9CP04542B.

[69] E. Prandini, E. Calì, A.G.P. Maloney, E. Parisi, E. Simone, Predicting particle quality attributes of organic crystalline materials using particle informatics, Powder Technol 443 (2024) 119927, https://doi.org/10.1016/j.powtec.2024.119927.

[70] E. Parisi, D. Del Duca, E. Prandini, S.F. Garofalo, C. Rosso, R.M. Chierotti, E. Simone, A combined experimental and modeling workflow to tune surface properties of organic materials via cocrystallization, Chem. Mater. (2025), https://doi.org/10.1021/acs.chemmater.5c00634.

[71] S. Benaglia, V.G. Gisbert, A.P. Perrino, C.A. Amo, R. Garcia, Fast and high-resolution mapping of elastic properties of biomolecules and polymers with bimodal AFM, Nat. Protoc. 13 (2018) 2890–2907, https://doi.org/10.1038/s41596-018-0070-1.

[72] M.F. Dupont, A. Elbourne, E. Mayes, K. Latham, Measuring the mechanical properties of flexible crystals using bi-modal atomic force microscopy, Phys. Chem. Chem. Phys. 21 (2019) 20219–20224, https://doi.org/10.1039/C9CP04542B.

[73] G. Clydesdale, R. Docherty, K.J. Roberts, HABIT — A program for predicting the morphology of molecular crystals, Comput. Phys. Commun. 64 (1991) 311–328, https://doi.org/10.1016/0010-4655(91)90040-R.

[74] G. Clydesdale, K.J. Roberts, R. Docherty, HABIT95 — A program for predicting the morphology of molecular crystals as a function of the growth environment, J. Cryst. Growth 166 (1996) 78–83, https://doi.org/10.1016/0022-0248(96)00056-5.

[75] K.J. Roberts, R.B. Hammond, V. Ramachandran, R. Docherty, Synthonic engineering, in: Y.A. Abramov (Ed.), Computational Pharmaceutical Solid State Chemistry, Computational Pharmaceutical Solid State Chemistry, 8, John Wiley & Sons, Hoboken, 2016, pp. 87–116, https://doi.org/10.1002/9781118700686.ch8.

[76] J.E. Sader, J.W.M. Chon, P. Mulvaney, Calibration of rectangular atomic force microscope cantilevers, Rev. Sci. Instrum. 70 (1999) 3967–3969, https://doi.org/10.1063/1.1150021.

[77] H. Jiang, S.M. Moosavi, J. Czaban-Jóźwiak, B. Torre, A. Shkurenko, Z.O. Ameur, J. Jia, N. Alsadun, O. Shekhah, E. Di Fabrizio, B. Smit, M. Eddaoudi, Reticular chemistry for the rational design of mechanically robust mesoporous merged-net metal–organic frameworks, Matter 6 (2023) 285–295, https://doi.org/10.1016/j.matt.2022.10.004.

[78] M. Heneczkowski, M. Kopacz, D. Nowak, A. Kuźniar, Infrared spectrum analysis of some flavonoids, Acta Pol. Pharm. 58 (2001) 415–420.

[79] S. Olejnik, A.M. Posner, J.P. Quirk, The IR spectra of interlamellar kaolinite–amide complexes—I. The complexes of formamide, N-methylformamide and dimethylformamide, Clays Clay Miner 19 (1971) 83–94, https://doi.org/10.1346/CCMN.1971.0190204.

[80] V. Venkata Chalapathi, K. Venkata Ramiah, Normal vibrations of N,N-dimethylformamide and N,N-dimethylacetamide, Proc. Indian Acad. Sci. Sect. A 68 (1968) 109–122, https://doi.org/10.1007/BF03049367.

[81] N.F.L. Machado, L.A.E. Batista de Carvalho, J.C. Otero, M.P.M. Marques, A conformational study of hydroxyflavones by vibrational spectroscopy coupled to DFT calculations, Spectrochim. Acta A Mol. Biomol. Spectrosc. 109 (2013) 116–124, https://doi.org/10.1016/j.saa.2013.01.038.

[82] M. Catauro, F. Papale, F. Bollino, S. Piccolella, S. Marciano, P. Nocera, S. Pacifico, Silica/quercetin sol–gel hybrids as antioxidant dental implant materials, Sci. Technol. Adv. Mater. 16 (2015) 035001, https://doi.org/10.1088/1468-6996/16/3/035001.

[83] R. Rajamohan, S. Ashokkumar, K. Murugavel, Y.R. Lee, Preparation and characterization of a nano-inclusion complex of quercetin with β-cyclodextrin and its potential activity on cancer cells, Micromachines (Basel) 14 (2023) 1352, https://doi.org/10.3390/mi14071352.

[84] G. Bakir, B.E. Girouard, R. Wiens, S. Mastel, E. Dillon, M. Kansiz, K.M. Gough, Orientation matters: polarization dependent IR spectroscopy of collagen from intact tendon down to the single fibril level, Molecules 25 (2020) 4295, https://doi.org/10.3390/molecules25184295.

[85] R. Mankar, C.C. Gajjela, C.E. Bueso-Ramos, C.C. Yin, D. Mayerich, R.K. Reddy, Polarization sensitive photothermal mid-infrared spectroscopic imaging of human bone marrow tissue, Appl. Spectrosc. 76 (2022) 1241–1252, https://doi.org/10.1177/00037028211063513.

[86] N. Baden, H. Kobayashi, N. Urayama, Submicron-resolution polymer orientation mapping by optical photothermal infrared spectroscopy, Int. J. Polym. Anal. Charact. 25 (2020) 1–7, https://doi.org/10.1080/1023666X.2020.1735851.

[87] P. Koziol, K. Kosowska, D. Liberda, F. Borondics, T.P. Wrobel, Super-resolved 3D mapping of molecular orientation using vibrational techniques, J. Am. Chem. Soc. 144 (2022) 14278–14287, https://doi.org/10.1021/jacs.2c05306.

[88] L. Mester, A.A. Govyadinov, S. Chen, M. Goikoetxea, R. Hillenbrand, Subsurface chemical nanoidentification by nano-FTIR spectroscopy, Nat. Commun. 11 (2020) 3359, https://doi.org/10.1038/s41467-020-17034-6.

[89] C.M. Reddy, K.A. Padmanabhan, G.R. Desiraju, Structure–property correlations in bending and brittle organic crystals, Nat. Commun. 4 (2013) 2829, https://doi.org/10.1021/cg060398w.

[90] M. Najib, R.B. Hammond, T. Mahmud, T. Izumi, Impact of Inequivalent Wetting on the Face-Specific Dissolution Rates for Single Faceted-Crystals Predicted from Solid-State Binding Energies, Cryst. Growth Des. 24 (12) (2024) 4894–4905, https://doi.org/10.1021/acs.cgd.2c00043.

[91] L. Attia, D. Nguyen, D. Gokhale, T. Zheng, P.S. Doyle, Surfactant–polymer complexation and competition on drug nanocrystal surfaces control crystallinity, ACS Appl. Mater. Interfaces 16 (26) (2024) 34409–34418, https://doi.org/10.1021/acsami.4c06815.

[92] G. Del Duca, E. Parisi, F. Artusio, E. Calì, S. Fraterrigo-Garofalo, C. Rosso, V. Cauda, M.R. Chierotti, E. Simone, A crystal engineering approach for rational design of curcumin crystals for Pickering stabilization of emulsions, Food Res. Int. 194 (2024) 114871, https://doi.org/10.1016/j.foodres.2024.114871.

[93] F. Collins, J.M. Skelton, S.L.M. Schroeder, H. Blade, M. Jackman, A.R. Pallipurath, Determination of the crystallographic orientation of organic crystal facets with angle-resolved polarised raman spectroscopy, Cryst. Eng. Comm. (2026), https://doi.org/10.1039/D5CE00672D.

[94] P. Gajjar, T.T.H. Nguyen, J. Sun, I.D. Styliari, H. Bale, S.A. McDonald, T.L. Burnett, et al., Crystallographic tomography and molecular modelling of structured organic polycrystalline powders, Cryst. Eng. Comm. (23) (2021) 2520–2531, https://doi.org/10.1039/D0CE01712D.

[95] Y. Wu, A.R. Chew, G.A. Rojas, G. Sini, G. Haugstad, A. Belianinov, S.V. Kalinin, H. Li, C. Risko, J.-L. Brédas, A. Salleo, C.D. Frisbie, Strain effects on the work function of an organic semiconductor, Nat. Commun. 7 (2016) 10270, https://doi.org/10.1038/ncomms10270.

[96] Z. Zhou, C. Qiao, J. Yao, Y. Yan, Y.S. Zhao, Exciton funneling amplified photoluminescence anisotropy in organic radical-doped microcrystals, J. Mater. Chem. C. 10 (2022) 2551–2555, https://doi.org/10.1039/D1TC02638K.

[97] H. Shi, Z. Li, S. Chen, Y. Yao, L. Wu, R. Shao, C. Sheng, S. Zhong, D. Wang, Y. Zhao, L. Zhao, S. Bai, Facet engineering of MOF supports regulates product selectivity in CO2 photoreduction by modulating electron and proton supply to COF shells, Chem. Sci. 16 (2025) 17688–17702, https://doi.org/10.1039/D5SC03122B.

[98] X.-M. Cheng, Y. Gu, X.-Y. Zhang, X.-Y. Dao, S. Wang, J. Ma, J. Zhao, W.-Y. Sun, Crystallographic facet heterojunction of MIL-125-NH2(Ti) for carbon dioxide photoreduction, Appl. Catal. B: Environ. 298 (2021) 120524, https://doi.org/10.1016/j.apcatb.2021.120524.